Journal of the Korean Ceramic Society
Vol. 26, No. 2, pp. 276 ~ 288, 1989.

Computer Image Simulation of γ-Al_2O_3 in High-Resolution Transmission Electron Microscopy

Jeong Y. Lee and R. Gronsky*
Department of Materials Science, Korea Institute of Technology
*MMRD, Lawrence Berkeley Laboratory
and
Department of Materials Science and Mineral Engineering, University of California, Berkeley
(Received February 11, 1989)

고분해능 투과전자현미경 연구에 의한 γ-Al_2O_3의 상 전산모사

이정용 · R. Gronsky*
한국과학기술대학, 전자재료과
*University of California, Berkeley
(1989년 2월 11일 접수)

요 약

요업체와 같은 복잡한 결정구조 또는 결함을 포함하고 있는 재료의 고분해능 전자현미경 상을 고신뢰성으로써 해석하기 위해서는 일반적으로 실험에서 얻어진 상과 전산모사로 얻어진 상을 비교한다.

산화알루미늄의 결정구조를 원자규모로 규명하기 위해서 고분해능 전자현미경사진을 촬영하고, 이것을 전산모사하여 실험에서 얻어진 상에서 산화알루미늄의 원자구조를 직접 알 수 있도록 하였다

실험결과, 실험에서 얻어진 상과 전산모사 상을 비교하고 분석함으로써 실험상의 어느 부분이 전산모사 원자모형 중의 어느 원자에 각각 대응이 되는지를 규명하였고, 스피넬 결정구조의 산화알루미늄에 있어서 알루미늄 원자는 팔면체 위치와 사면체 위치 모두에 무질서하게 존재함을 밝혀냈다.

ABSTRACT

Interpretation of high-resolution transmission electron microscopy images of defects and complex structures such as found in ceramics generally requires matching of the images with computed image simulations for reliable interpretation.

A transmission electron microscopy study of the aluminum oxide was carried out at high-resolution, so that the crystal structure of the aluminum oxide could be modelled on an atomic level. In conjunction with computer simulation comparisons, the images reveal directly the atomic structure of the oxide.

Results show that comparison between experimental high-resolution electron microscopy images

and simulated images leads to a one to one correspondence of the image to the atomic model of the aluminum oxide. The aluminum atoms are disordered in the octahedral sites and the tetrahedral sites in the spinel aluminum oxide.

1. INTRODUCTION

The current generation of electron microscopes makes possible the attainment of atomic resolution in the image of crystals.[1] However, the image contrast in the high-resolution electron micrographs varies rapidly with objective lens focus and specimen thickness. Only for very thin specimens, typically less than 5-10 nm for many oxide and silicate minerals, and a few tens of Angstroms for most metals and alloys, and for selective settings of defocus does the image contrast bear a one to one correspondence to the specimen structure.[2] For specimens thicker than the above limits, there is no simple relationship between the image and the projected specimen structure. To provide proper interpretation of the image it is usually necessary to match experimental images to computer simulated images for a range of defocus values and specimen thickness. In particular, interpretation of images of defects (e.g. interfaces) and complex structures such as found in ceramics generally requires matching of the images with companion computed image simulations for reliable interpretation.

1.1 Theory of Image Simulation

The starting point for image formation is to model the electron microscope as a simple system of electron beam, specimen and lens system (Fig. 1). Generally the initial electron beam is considered to be a parallel beam of plane wave electrons. The microscope lens system is replaced by one spherically-aberrated lens which can be regarded as representing the objective lens. In a real electron microscope, the objective lens has the crucial duty of reassembling the diffracted beams emerging from the specimen into the image, which is merely magnified further by subsequent lenses.

In any simulation three functions representing the electron wave amplitude must be computed at the three positions within the model microscope; at the exit surface of the specimen, $\psi(x)$, at the back-focal plane of the objective lens, $F(\mathbf{k})$; and the image plane of the lens, $\Psi(x)$.

The computation of the exit-surface wave $\psi(x)$, involves mainly the model specimen structure (the only microscope parameter involved is the energy of the electrons in the incident beam). The wave at the back-focal plane, $F(\mathbf{k})$, is obtained via a simple Fourier transform of the exit-surface wave $\psi(x)$. Calculation of the image from the electron wave at the diffraction plane does not involve the specimen, but only microscope parameters, such as objective lens defocus and spherical aberration. Together with the objective aperture size and position, these modify $F(\mathbf{k})$ before it is transformed, into $\Psi(\mathbf{x})$, the image amplitude.

Current image simulation calculations are usually based on the multislice method[3] in which the amplitude and phase at the exit-surface of a crystalline specimen is found by treating the crystal as consisting of N slices of thickness Δz so that the total thickness $t = N\Delta z$. The crystal potential of each slice is then replaced by the two dimensional projected potential for sufficiently small Δz. The effect of the first slice on the incident wave is calculated: the resulting wavefunction is then propagated through free space to the next slice. This is repeated until the desired thickness is achieved.

First, a calculational unit cell is selected

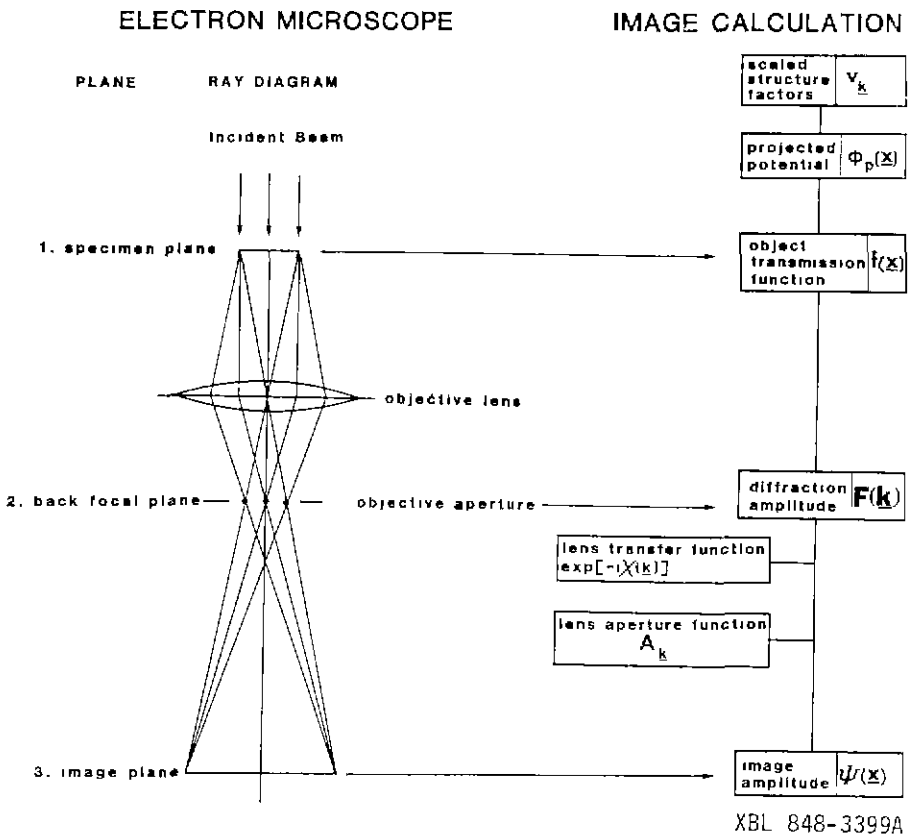

Fig. 1. A pictorial guide for the discussion of the various steps in the calculation of a HRTEM image (after Reference 4).

with specification of atomic species and coordinates. The Fourier coefficients of potential (structure factors) at the reciprocal lattice points are calculated by summing over all atoms in the unit cell:

$$V_{\mathbf{k}} = \frac{h^2}{2\pi m_e e V_c} \sum_j e_{f_j} | \mathbf{k} | \exp(-2\pi i\, \mathbf{k}\cdot\mathbf{r}_j)$$

where V_c is the volume of the unit cell, j identifies the atoms in the unit cell, e_f and $\mathbf{r}$ are the electron scattering factors and the positions of the atoms, respectively, $\mathbf{k}$ gives a reciprocal lattice position, $\mathbf{k} \equiv [u,v]$, and the other terms have the usual meaning. The electron scattering factor, which is defined as the Fourier transform of the potential distribution for each atom, can also be computed from experimental X-ray structure factors. Inclusion of all $V_{\mathbf{k}}$ within 40 nm^{-1} of the origin of reciprocal space provides sufficient accuracy for most calculations.[4]

Fourier transformation of the $V_{\mathbf{k}}$ values produces $\phi_p(\mathbf{x})$ the crystal potential of one unit cell projected in the direction of the electron beam. The effect of such a thin *slice* of crystal on the electron beam is that of a phase object, and the electron *transmission function* for the slice is

$$q(\mathbf{x}) = \exp[i\sigma\phi_p(\mathbf{x})\Delta z]$$

where Δz is the *slice thickness* and σ is the interaction parameter for the electrons of the designated energy

The exit-surface wave at the desired crystal

thickness, $t = m\Delta z$, is found from $q(\mathbf{x})$ by iteration. After m slices the electron wave $\psi(\mathbf{x})$ is given by

$$^{m}f(\mathbf{x}) = [^{m-1}f(\mathbf{x}) * {}^{m}p(\mathbf{x})]\ {}^{m}q(\mathbf{x})$$

where $^{m}q(\mathbf{x})$ is the transmission function of the mth slice and $^{m}p(\mathbf{x})$ is the small-angle approximation to the free space propagator for the distance between the $(m$-1)th and mth slices (i.e. the familiar Fresnel propagator), $*$ represents the convolution operation.

The diffraction plane wavefield $^{m}F(\mathbf{k})$ is obtained from $^{m}f(\mathbf{x})$ by Fourier transformation. In fact, the multislice is typically carried out in reciprocal space, leading directly to $F(\mathbf{k})$

$$^{m}F(\mathbf{k}) = [^{m-1}F(\mathbf{k})\ {}^{m}P_{\mathbf{k}}] * {}^{m}Q_{\mathbf{k}}$$

where $P_{\mathbf{k}}$ and $Q_{\mathbf{k}}$ are the Fourier transforms of $p(\mathbf{x})$ and $q(\mathbf{x})$.

In order to compute the image plane intensity of the image-plane wave, one needs to include the effects of objective lens defocus and spherical aberration. These parameters act merely to change the phases of the diffracted electron beams passing through the aperture of the lens. Thus, the modified back-focal plane wavefield becomes;

$$F_m(\mathbf{k}) = F(\mathbf{k})A_{\mathbf{k}}\exp[i\chi(\mathbf{k})]$$

where χ is the phase shift relative to the optic axis. The objective aperture function $A_{\mathbf{k}}$ is unity for beams passing through the aperture and zero for those outside.

The convergent character of the incident electron beam and the spread of focus produced by the energy spread in the incident electrons have the effect of smearing the microscope image by making it a composite of high-resolution images. Incident beam convergence produces composite images formed by the summation of the many images, each at a different angle within the incident cone. Spread of focus produces a composite formed from images summed over a range of defocus These influences can be taken into account by modifying the back-focal plane wavefield.

Whereas an accurate value of the beam convergence α can be measured directly from a diffraction pattern obtained with focussed illumination, the spread of focus Δ for a particular electron microscope must either be estimated by matching an experimental image with ones computed using different values of Δ, or approximated from known values of the chromatic aberration coefficient C_C and high voltage and lens current ripple.

Lastly, the simulated image, i.e. the intensity in the image plane, can be calculated by a Fourier transform of the fully modified back-focal plane wavefield to obtain the amplitude $\Psi(\mathbf{x})$ followed by squaring of the amplitude:

$$I(\mathbf{x}) = \Psi(\mathbf{x})\cdot\Psi^{*}(\mathbf{x}).$$

1.2 Crystal Structure of γ-Al_2O_3

This phase has a defect spinel structure with the oxygen ions in face-centered cubic close packing and the aluminum ions in certain interstices. The lattice parameter of γ-Al_2O_3 is 0.79 nm[5] and the atomic radius of Al^{3+} is 0 051 nm while that of O^{2-} is 0.140 nm.[6]

As shown in Fig. 2, for an elementary cell

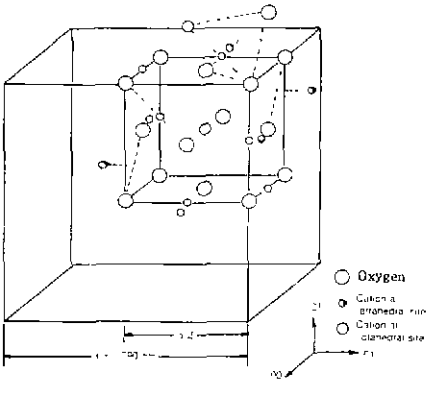

Fig. 2. Crystal structure and lattice parameter of the spinel oxide, γ-Al_2O_3 at room temperature.

of this spinel structure there are four oxygen atoms, four octahedral interstices, and eight tetrahedral interstices. This makes a total of twelve intersticies to be filled by three cations. In each elementary cell two octahedral sites are filled and one tetrahedral. Eight of these elementary cells are arranged so as to form a unit cell containing 32 oxygen ions, 16 octahedral cations, and 8 tetrahedral cations as illustrated in Fig. 2.

In γ-Al_2O_3, there are $21\frac{1}{3}$ aluminum cations in the unit cell of 32 oxygen ions to maintain charge balance, so $21\frac{1}{3}$ aluminum ions are distributed among the 24 cation sites. There is considerable disagreement[7), 8), 9)] as to the distribution of aluminum ions in the cation sites of the spinel structure. Generally the distribution depends significantly on the history of the preparation of the sample. Furthermore, noncubic γ-Al_2O_3 with a tetragonal distortion was found in the case of decomposition of aluminum hydrates.[10)]

The idea that reorganization of the cation distribution in a defect NaCl-type intermediate might lead ultimately to the spinel structure suggests that initially in a defect Al_2O_3 spinel the vacancies are on tetrahedral sites.[10)] Evidence in the literature on the positions of vacancies in γ-Al_2O_3 is not available, although Leonard *et al* [9)] have demonstrated for a series of heat-treated alumina gels that radial electron density distribution functions can provide information on cation distributions. Saalfeld[8)] considered that vacancies in γ-Al_2O_3 are probably on tetrahedral sites. He suggested further that the tetragonal distortion of γ-Al_2O_3 and the shortened *c* axis are due to a cation distribution in which octahedral sites are predominantly occupied

Lippens and de Boer[11)] observed streaking of [110] electron diffraction pattern. They concluded from structure factor considerations that this revealed considerable disorder in the occupation of the tetrahedral sites. Sinha and Sinha[12)] considered the nature of vacancy distribution in the defect spinel-type oxides in the light of the available magnetic and structural data. They concluded that the vacancies are randomly distributed among the octahedral and tetrahedral positions.

2. EXPERIMENTAL PROCEDURES

2.1 Specimen Preparation for Transmission Electron Microscopy

The 99.999 % pure polycrystalline and single crystal aluminum were used. The aluminum ingot was cut into coupons of 1.4 mm×2.5 mm×2 mm in order to be mounted on a copper grid.

For the clean and flat surface preparation, the sample was mechanically polished and chemically etched in sodium hydroxide, dipped into nitric acid and washed in anhydrous methanol. The sample was stored in an atmospheric pressure desiccator for 1 day to allow formation of a uniform room temperature oxide, and then oxidized in 1 atm air at 600°C for 4 weeks.

The sample was mounted with wax (80°C melting point) onto a quartz disc. The sample was polished mechanically on a rotating wheel with 600 grit paper to remove the aluminum metal which was not oxidized. The sample was separated from the quartz disc by dissolving the wax in a beaker of ethanol The sample was then dried and glued to a copper grid for support and eacy handling.

The rotating specimen stage of the Gatan ion mill, cooled with liquid nitrogen, was used for ion beam milling at 17° gun tilt, 5 kV gun voltage and 50 μA specimen current. The final milling was accomplished with at 12° gun tilt,

10μA specimen current.

2.2 High-Resolution Transmission Electron Microscopy

The microscope for this study was the JEOL JEM 200CX (high-resolution pole piece, spherical aberration coefficient; C_S = 1.2 mm, C_C = 1.4 mm at 200 keV).

Generally, the filament (LaB_6) was operated with a brighter central spot in an undersaturated mode in order to increase beam coherence.[13] The first condenser lens was turned off to enhance brightness and the condenser aperture was inserted for optimum trade-off between brightness and beam coherence. Following careful alignment of the imaging system, the specimen was tilted using a combination of the extinction contours in the bright-field (BF), and Kikuchi lines and the high-order Laue zone (HOLZ) lines to produce the highest symmetry in diffraction pattern corresponding to the <110> zone axis.

The beams corresponding to reciprocal lattice vectors with magnitude greater than the reciprocal space position at the point-to-point resolution limit will contribute only to the background noise in the image. Choosing a suitable objective aperture can exclude these beams, thereby improving image contrast.

At the correct stigmator setting, the amorphous region should show fine grain non-directional contrast as the focus is taken above and below the minimum contrast condition. The objective lens current is then adjusted to obtain an image with minimum phase contrast. This establishes the minimum contrast condition (Δf_{min}), where image shift due to spherical aberration has been offset by an objective lens at underfocus (Δf) from the Gaussian image plane (Δf=0) given by $\Delta f_{min} = -0.44\ C_S\lambda^2$, where λ is the wavelength. Since this is easily observed and calculated for known C_S and λ, it serves as reference point, from which the objective lens can be defocussed in set increments to reach the optimum focus condition.

Exposures of 4 sec at 530 kx magnification were generally used. Amorphous edges were included in the images to obtain information about defocus, astigmatism and specimen drift by optical diffraction of the developed negative on a laser bench.

2.3 Image Simulations

Simulated high-resolution electron microscope lattice images are calculated on the Lawrence Berkeley Laboratory (LBL) Control Data Corp. 7600 computer using the LBL MSLICE programs developed by R. Kilaas.[14] These programs at LBL are able to compute scattering factors, perform multislicing, simulate the effect of the microscope lenses, plot images as gray level plots, plot projected slice potentials, compute and plot diffraction patterns, plot amplitudes and phases of selected beams as a function of thickness and plot contrast transfer functions. The LBL MSLICE computer simulation programs for an image consist of three programs, PHSGR, MULTI, DISPL. They are run in succession and each of these programs except PHSGR uses the output of the previous program plus its own input file containing additional operating parameters to calculate the final image. PHSGR calculates the effective potential seen by the electron as it moves through the specimen, MULTI then calculates the electron distribution as a function of specimen thickness after the actual propagation of the electron through the specimen and DISPL calculates the interaction between the electrons and the imaging system of the microscope before synthesizing the final image. Each of these programs, and the values commonly used as input parameters in this study are described briefly below.

2.3.1 PHSGR

PHSGR calculates the effective potential from electron scattering factors which are cal-

culated using relativistic Hatree-Fock atomic wave functions.[15] In principle the potential should include all scattering processes, both elastic and inelastic However, in practice only elastic scattering is usually included

The typical parameters as input to PHSGR are the simulation cell dimensions (A, B and C), atom positions, the atomic numbers of species, the number of atoms, the space group symmetry operators, isotropic temperature factors and the projection directions. In this study, all images were simulated with the electron beam incident along the <110> direction, since all the high-resolution images were taken along this direction. For a perfect crystal, one simply selects some multiple of the crystal unit cell parameters in the x and y directions respectively for A and B as shown in Fig. 3 (a). In effect, the programs calculate an image for a periodic array of the unit cells as shown in Fig. 3 (a), the so-called *periodic extension* method. The use of Fourier transforms requires that the unit cell be smoothly varying at the boundaries. The input file, including atom positions of Al (atomic number 13, isotropic temperature factor 0.3) and O (atomic number 8, isotropic temperature factor 0.7), was used.

2.3.2 MULTI

The part of the computation, which treats the interaction between the specimen and the electron beam, is mostly based upon a dynamical multislice formulation proposed by Cowley-Moodie.[16] This calculation involves solving the one-electron Schrödinger equation. Beginning with the known electron distribution at the top of the specimen, MULTI calculates the electron wave function at each slice from the wave function at the previous slice, and stacks these outputs to produce the multi-slice scattered wave from a thick crystal. Output from thicknesses of interest are saved for final input to DISPL The important values input for MULTI -e the accelerating voltage of the microscope

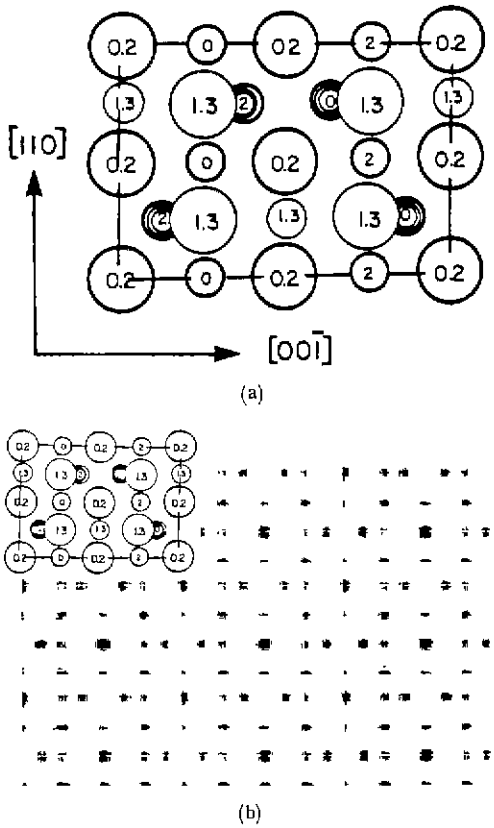

Fig. 3. (a) Unit cell used for a 3×3 periodic array of the unit cells for computer image simulations of the crystalline oxide assuming that the aluminum ions are disordered in the octahedral sites and the tetrahedral sites.
b) Projected potential for the atomic model. The atom positions are superimposed on the figure in the top-left corner. The potential contains 3×3 unit cells of the unit cell (a).

(200 keV for the JEOL JEM 200CX), the phase grating slice thickness, sampling points of beams to be used in the multislice calculation and the the coordinates (h,k) of the Laue circle center, to distinguish whether the electron beam is tilted with respect to the crystal, or vise-versa. In this image simulation, calculations are performed using 256×256 sampling points and the coordinates $(h = 0,\ k = 0)$ of the Laue circle center

2.3.3 DISPL

DISPL combines the beams from MULTI in a Fourier series to form the electron lattice image, taking into account the effects of the imaging system of the microscope. DISPL plots images as gray level plots to dispose the simulated image intensities using the Varian Plotter at the LBL Computer Center. The important microscope parameters and typical values for the JEOL JEM 200CX that were used as input for DISPL are spherical aberration coefficient (C_S = 1.2 mm), semi-angle of illumination (α = 1 0 mrad), half-width of Gaussian spread of defocus (Δ = 5 nm), objective lens defocus (Δf = +36 to −300 nm), radius of objective aperture (5 nm^{-1}), h,k coordinates of the optic axis and objective aperture center (0,0).

3. RESULTS AND DISCUSSION

3.1 Experimental High-Resolution Image of γ-Al_2O_3

Figure 4 shows a low-magnification of experimental high-resolution electron microscopy images of γ-Al_2O_3 in the sample which was oxidized for 2 weeks at 600°C. The edge of the specimen is off to the top of the micrograph, i.e. the sample thickness is decreasing from the bottom to the top in the micrograph. The image character of the oxide is shown in greater detail in the enlargements in Figs. 5 (a)-(d) corresponding to the images from the thick area to the thin area in Fig. 4. From these enlargements, it is readily apparent that there are significant changes in the contrast due to the specimen thickness changes although all the micrographs in this figure were taken at the same defocus setting. The sensitive contrast change with specimen thickness is due to the fact that relatively many beams of the oxide in the reci-

Fig. 4 High-resolution transmission electron microscopy image of [1 $\bar{1}$ 0] γ-Al_2O_3.

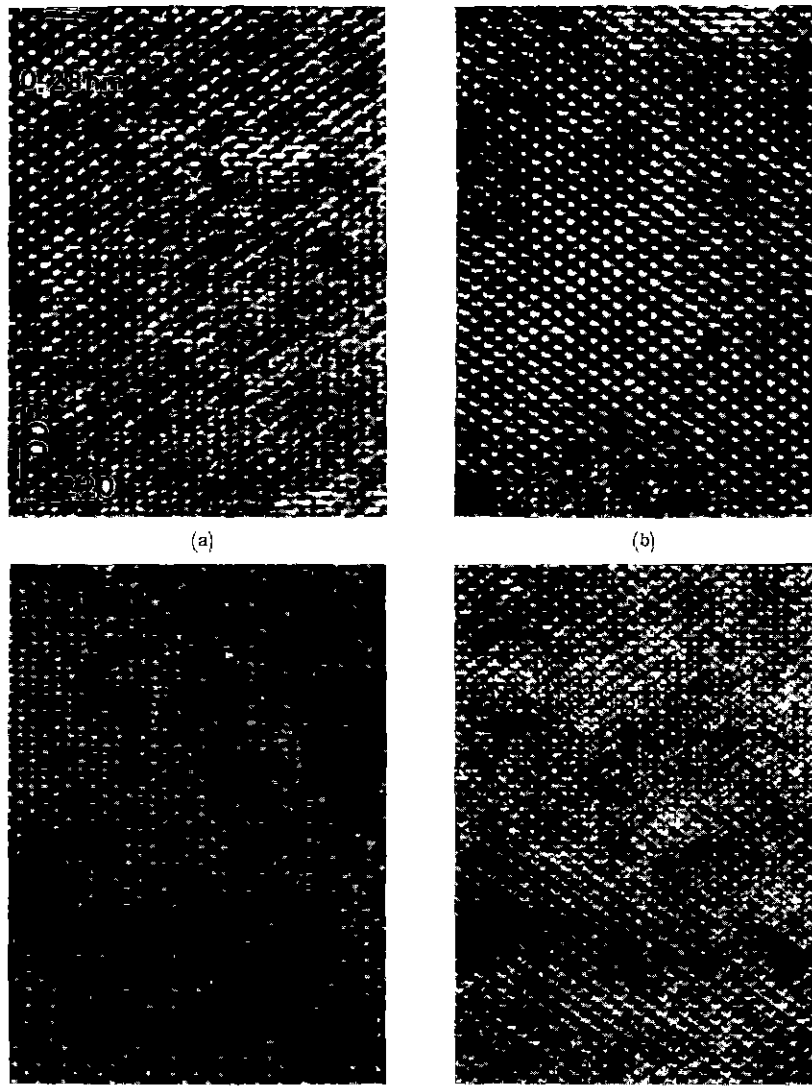

(a) (b) (c) (d)

Fig. 5 (a) – (b) Enlargements from γ-Al_2O_3 in Fig. 4

procal space contribute the image forming process, and the local contrast change is due to the fact that there may be local thickness variations in the specimen, defects in the oxide, or overlayer on the surface due to the amorphous oxide or the specimen contamination.

3.2 Image Calculation for γ-Al_2O_3 Structure

The main purpose of this section is to examine simulated high-resolution transmission electron microscopy (HRTEM) images of the γ-Al_2O_3 crystal structure in order to know how variations of specimen thickness and objective lens defocus value affect the appearance of these images. This information will then indicate if HRTEM images can be used to estimate the specimen thickness and defocus value, by com-

paring simulated images and experimental images.

The actual atom positions used for image simulations are shown in Fig. 3, where it was assumed that the aluminum atoms are distributed at random in the octahedral sites and the tetrahedral sites. In this figure, the oxygen atoms are represented by large circles, and the aluminum atoms at the octahedral or tetrahedral sites are represented by small single or triple circles, respectively. Numbers in the circles show the relative heights of atoms in multiples of $\frac{a}{8}[1\bar{1}0]$. Ions are drawn in thick lines when the height is an even number and in thin lines when the height is an odd number. This calculational unit cell contains 3x3 unit cells of the unit cell shown in the top of Fig. 3

Figure 3 (b) shows the projected potential for the calculational unit cell. Notice from this projected potential that the atom positions, which contain two aluminum atoms along the projected direction, have a much larger projected potential than those, which contains one aluminum atom, although the projected potentials of two oxygen atoms are still slightly larger than the projected potentials of one aluminum atom in the calculational unit cell. This is due to the fact that the projected potentials of atoms increases with scattering factor and the density of the atoms. The high scattering factor of Al atoms as compared to O atoms leads to the different sizes of the projected potential. There are small mismatches of the projected potentials at the unit cell boundaries due to the incomplete printing of the computer printer. However, this fact does not affect the present image simulations because all the actual calculations were done for the perfect projected potentials.

A series of calculated images from the projected potential shown in Fig. 3, as a function of both objective lens defocus and specimen thickness up to 25 nm, is shown in Fig. 6, where the atom positions of the unit cell are also shown superimposed in the upper-left corners of simulated images at each defocus value.

Notice that simulated images show relatively good contrast over a wide range of defocus values, because many spatial frequencies for 31 beams including the (111), (200) and (220) reflections from the oxide specimen contribute the image formation in the objective aperture, although the contrast transfer functions do not always transfer well all the spatial frequencies. Also notice that only subtle changes in objective lens defocus accompany the relatively large changes in contrast because many spatial frequencies affect the image formation by the variations of the contrast transfer functions with lens defocus values. In addition, there is a similar contrast change in the appearance of the images with thickness.

3.3 Comparison of Experimental HRTEM images with Simulated Images

Thus, these image simulations indicate that it is possible to estimate objective lens defocus value and specimen thickness for experimental images by comparing experimental and simulated images. Note that, whereas it is possible to determine the objective lens defocus from a HRTEM negative to the accuracy needed for correct image interpretation by using an optical bench, it is extremely difficult to measure the specimen thickness in the very thin areas where HRTEM images are most interpretable.

Figure 7 shows an enlarged experimental HRTEM image of a γ-Al_2O_3 crystal from Fig. 4. Note that all of the high-resolution lattice images were taken with a <110> electron beam direction in this study. Notice that the bright spots in this image are arrayed in a rectangular pattern. Comparison of this image contrast with a series of simulated images in Fig. 6 shows that good agreement is obtained for a specimen thickness 25 nm and at objective lens defocus setting of

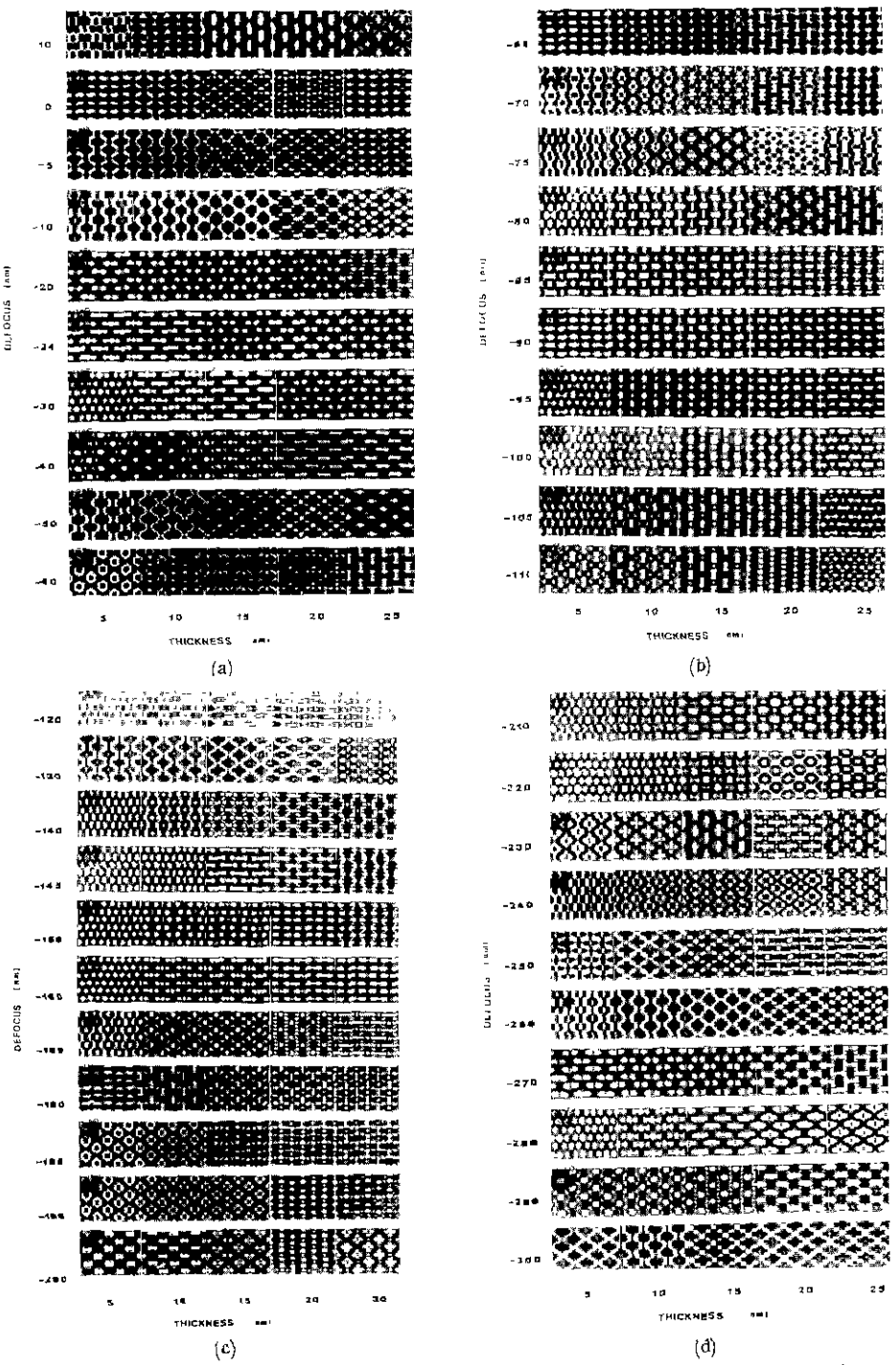

Fig. 6 (a)–(b) A series of simulated high-resolution transmission electron microscopy images of the γ-Al_2O_3 atomic model in Fig. 3 shown as a function of objective lens defocus, from 10 to −300 nm, and specimen thickness, from 5 to 25 nm. The atom positions are superimposed in the top-left corner at each defocus setting.

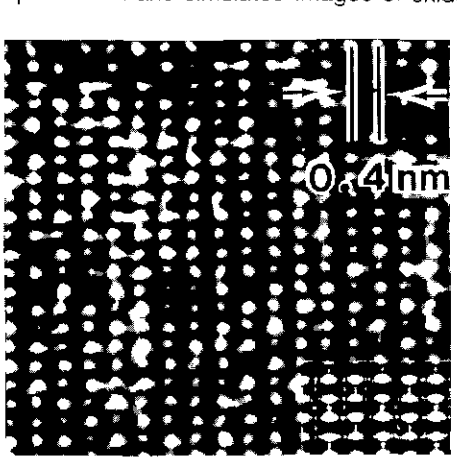

Fig. 7. *Experimental and simulated HRTEM images of* γ-Al_2O_3 in a <110> orientation. Note the matching between the experimental image and the inset superimposed simulated image of the oxide at −66 nm defocus and 25 nm thickness from Fig 6

−66 nm. This fact is clearly illustrated by the inset calculated HRTEM image of γ-Al_2O_3 crystal, obtained under imaging conditions of −66 nm defocus and 25 nm thickness, as shown in the bottom-right corner of this image. Notice the excellent agreement between these two images, further substantiating the validity of the model in Fig. 3, i.e. the aluminum atoms are disordered in the octahedral sites and the tetrahedral sites in the spinel oxide. Furthermore, the bright spots in the experimental HRTEM image in Fig. 7 correspond to some of the oxygen atoms in the atomic model in Fig. 3 (a) and the locations of other atoms can be identified by matching of the experimental image with the calculational unit cell model.

4. CONCLUSIONS

A transmission electron microscopy study of the aluminum oxide was carried out at high-resolution, so that the crystal structure of the aluminum oxide could be modelled on an atomic level. In conjunction with computer simulation comparisons, the images reveal directly the atomic structure of the oxide. The following results have been obtained:

1. Comparison between experimental high-resolution electron microscopy images and simulated images leads to a one to one correspondence of the image to the atomic model of the aluminum oxide.
2. The aluminum atoms are disordered in the octahedral sites and the tetrahedral sites in the spinel aluminum oxide.

ACKNOWLEDGEMENTS

This research was partially supported by the Director, Office of Energy Research, Office of Basic Energy Sciences, Materials Science Division of the U.S. Department of Energy under Contract No. DE-AC03-76SF00098.

REFERENCES

1 R Gronsky, "The U.S. Atom-Resolving Microscope Project," in *38th Ann. Proc. Electron Microscopy Soc. Amer.*, ed. by G W Baily, San Francisco Press, San Francisco, CA, 2 (1980).
2. J.C.H. Spence, *Experimental High-Resolution Electron Microscopy*, Clarendon Press, Oxford, 86 (1981).
3 P Goodman and A.F. Moodie, "Numerical Evaluation of n-beam Wave Functions in Electron Scattering by the Multi-slice Method," *Acta Cryst.*, **A30**, 280 (1974)
4. M A O'Keefe, "Electron Image Simulation: A Complementary Processing Technique," in *Electron Optical Systems*, SEM Inc., AMF O'Hare (Chicago), 209 (1985).
5. G. Hass, "Growth and Structure of Thin Oxide Layers on Aluminum," *Optik*, **1**, 134 (1946).

6. L. Pauling, *The Nature of Chemical Bond,* Cornell Univ. Press, Ithaca, New York, 220 (1960).
7. S.J. Wilson, "Phase Transformations and Development of Microstructure in Boehmite-derived Transition Aluminas," *Proc. Brit. Ceram. Soc.*, **69**, 85 (1970).
8. H. Saalfeld, "Dehydration of Gibbsite and the Structure of a Tetragonal γ-Al_2O_3," *Clay Min. Bull*, **3**, 249 (1958)
9. A.J. Leonard, F. Van Cauwelaert and J.J. Fripiat, "Radial Electron Density Distribution Functions of Alumina Gels," *J. Phys. Chem.*, **71**, 695 (1967).
10. S.J. Wilson, "The Dehydration of Boehmite, γ-AlOOH, to γ-Al_2O_3," *J. Solid State Chem.*, **30**, 247 (1979).
11. B.C. Lippens and J H. de Boer, "Study of Phase Transformations During Calcination of Aluminum Hydroxides by Selected Area Electron Diffraction," *Acta Cryst.*, **17**, 1312 (1964).
12. K.P. Sinha and A P B. Sinha, "Vacancy Distribution and Bonding in Some Oxides of Spinel Structures," *J. Phys. Chem.*, **61**, 758 (1957).
13. R Gronsky, "High-Resolution Transmission Electron Microscopy," in *Treatise on Materials Science and Technology: Experimental Techniques, 19B,* Academic Press, New York, 325 (1983).
14. R. Kilaas, "Computer Simulation of High-Resolution Transmission Electron Micrograph: Theory and Analysis," Ph.D. Thesis, University of California, Berkeley, LBL-19058 (1985).
15. P.A. Doyle and P.S. Turner, "Relativistic Hatree-Fock X-ray and Electron Scattering Factors," *Acta Cryst.*, **A24**, 390 (1968).
16. J.M. Cowley and A.F. Moodie, "The Scattering of Electrons by Atoms and Crystals. I. A New Theoretical Approach," *Acta Cryst.*, **10**, 609 (1957).